Multi-scale analysis of a viscoelastic liquid jet

Christophe Tirel, Marie-Charlotte Renoult, Christophe Dumouchel, Denis Lisiecki, Olivier Crumeyrolle, Innocent Mutabazi

Multi-scale analysis of a viscoelastic liquid jet

Christophe Tirel[a], Marie-Charlotte Renoult[a,b,*], Christophe Dumouchel[a], Denis Lisiecki[a], Olivier Crumeyrolle[b], Innocent Mutabazi[b]

[a]Normandie Université, Université et INSA de Rouen, CNRS – CORIA, 76801 Saint-Etienne du Rouvray, France

[b]Normandie Université, Université du Havre, CNRS – LOMC, 76053 Le Havre, France

Abstract

A multi-scale analyzing tool is now available to investigate the temporal evolution of two phase flows such as liquid systems experiencing an atomization process. Thanks to its multi-scale and global nature, it allows identifying all dynamics simultaneously involved in the process with no restriction of the liquid system shape. In the present work this multi-scale tool is applied on 2D visualizations of free falling jets of a low-viscosity viscoelastic solution. The jets are produced from a cylindrical discharge orifice and the liquid is a very dilute polymer solution containing 5 PPM of Poly(ethylene oxide). High spatial resolution images of the free falling jets are performed as a function of the velocity and at several distances from the discharge orifice. For every operating condition, the liquid jet remains cylindrical first, then shows the development of a sinusoidal perturbation and finally adopts a beads-on-a-string pattern before breakup occurs. The multi-scale analysis is performed on a high number of images and at several spatial positions in order to return statistical and temporal information, respectively. The results of this analysis show that during the sinusoidal perturbation stage, the large-scale region follows an exponential increase as predicted by the linear stability theory and during the beads-on-a-string

stage, the small-scale region follows an exponential decrease similar to an elasto-capillary regime from which the relaxation time of the polymer solution can be extracted. This work positions the multi-scale approach as a promising and complementary tool to the currently used techniques in order to probe complex liquid rheology, especially in the case of mobile viscoelastic solutions.

Keywords: Multi-scale analysis; Extensional rheology; Jet break-up; Low-viscosity viscoelastic liquids; Dilute polymer solutions

Nomenclature

$D(d,t)$	µm	Scale diameter
d	µm	Scale
d_1	µm	Specific small scale
$D_c(t)$ $D_s(t)$	µm	Cylinder and sphere diameter
D_{c0}, D_{s0}	µm	Initial cylinder and sphere diameter
De	-	Deborah number
D_j	µm	Jet diameter
D_{max}	µm	Jet diameter of the maximum surface point
d_{max}	µm	Maximum scale
D_{min}	µm	Jet diameter of the minimum surface point
D_{or}	µm	Discharge orifice diameter
D_{sfin}	µm	Final sphere diameter
$E_2(d,t)$	-	Cumulative scale distribution
$e_2(d,t)$	μm^{-1}	Scale distribution
Fr	-	Froude number
g	$m.s^{-2}$	Gravity acceleration constant
H_w	pixel	Analyzing window height
k	mm^{-1}	Perturbation wavenumber
L	µm	Cylinder length
L_{BU}	mm	Average breakup length
L_{or}	µm	Discharge orifice length
M_v	$g.mol^{-1}$	Molar mass
Oh	-	Ohnesorge number

R	$J.mol^{-1}.K^{-1}$	Gas constant
Re	-	Reynolds number
S_T	mm^2	Total surface area of the liquid system
$S(d)$	mm^2	Surface area of the eroded system at scale d
t	ms	Time
t_{BU}	ms	Breakup time
t_r	ms	Relaxation time of the polymer solution
t_σ	ms	Capillary time
T	K	Temperature
V_q	$m.s^{-1}$	Mean jet velocity
We	-	Liquid Weber number
z	mm	Distance from nozzle orifice
ΔH_w	pixel	Analyzing window shift
λ	mm	Perturbation wavelength
μ	Pa.s	Shear viscosity
$[\mu]$	ppm^{-1}	Polymer intrinsic viscosity into the solvent
ρ	$kg.m^{-3}$	Liquid density
σ	$N.m^{-1}$	Surface tension coefficient
ω	s^{-1}	Growth rate of the jet instability

1 Introduction

A falling jet issuing from an orifice into atmospheric air is an example of a two-phase flow with evolving interface shapes. It also makes a wonderful case study of a capillary-driven fluid instability [1, 2]. Any surface deformation of wavelength greater than the jet circumference is capillary unstable and grows along the jet axis, causing the jet breakup. During this process, the falling jet deforms into swollen regions connected by filaments until final breakup. The jet interface is thus a complex time-dependent shape function. After breakup, jet fragments tend to rearrange themselves into spherical drops, which is the shape minimizing the surface area and also the surface energy provided that the surface tension is constant, of a given liquid volume.

Capillary jets are widely present in Nature as well as in various industrial and medical applications (see [3] for a detailed review on the physics of the jet). Because of the fundamental and industrial interest of capillary jets, there are numerous experimental and numerical studies dedicated to the jet problem, exploring more or less complex configurations. Increasingly the complexity concerns the nature of the liquid.

The measurements commonly performed on capillary jets are the wavelength of the perturbation and the temporal evolution of its amplitude. These measurements require a prior detection of the interface minimum/maximum displacements from its unperturbed state [4]. Quite often this detection is made easier by imposing the perturbation frequency that annihilates the temporal and spatial variabilities of the jet behavior [5]. This constraint may be skipped by using a multi-scale tool such as the one recently introduced to describe and analyze time-dependent fluid domains in atomization processes [6-8]. In this technique, any fluid region delimited by an interface is described by a scale distribution that is measured as a function of time. This allows us to identify characteristic and distinct scale behaviors for characteristic scales and time periods in one single measurement. The purpose of the present work is to apply this global and easy to use technique on experimental visualizations of free falling capillary jets

of a viscoelastic solution in order to measure the dynamic of their large and small-scale structures. This approach is inspired from a recently multi-scale analysis of simulated capillary instability of a forced Newtonian liquid jet [9]. In that analysis, the temporal evolution of two characteristic scales was examined: the maximum scale d_{max} and the scale d_1. d_{max} is representative of the drop region and is equal to the diameter of the maximum surface point $D_{\max}$. d_1 is not equal to the minimum surface point D_{min} but its dynamics is the same. Therefore, the method gives access to the dynamics of D_{max} and $D_{\min}$ through d_{max} and d_1, respectively. The time evolution of d_{max} was shown to be exponential as expected by linear stability theory. The relation between d_{max} and time t reads:

$$\frac{d_{\max}}{D_j} = 1 - 2\eta_m \exp\left(\omega_m \frac{t}{t_\sigma}\right) \tag{1}$$

Here D_j is the unperturbed jet diameter and $t_\sigma = \sqrt{\rho D_j^3 / (8\sigma)}$ is the capillary time. ρ and σ are the density and air/liquid surface tension, respectively. The growth rate ω_m and the amplitude parameter η_m both depend on the perturbation wavelength. ω_m was found in excellent agreement with the prediction of linear stability theory [9]. On the other hand, the scale d_1 follows three regimes of evolution: an exponential regime, a power-law regime and a linear one in agreement with previous studies on capillary liquid breakup (see for instance the map of misery of Clasen et al. [10]). The first regime is the counterpart of the exponential increase of d_{max} while the last two ones correspond to two thinning regimes, differing only by the dominant resisting force acting against the capillary-driving one: inertia then viscosity. In the inertia-capillary regime the evolution of d_1 writes:

$$\frac{d_1}{d_1^*} = \left(1 - \omega^* \frac{t - t^*}{t_\sigma^*}\right)^{2/3} \tag{2}$$

where $t_\sigma^* = \sqrt{\left(\rho d_1^{*3}\right)/\left(8\sigma\right)}$ and the parameters d_1^*, ω^*,t^* depend on the perturbation wavelength. In the visco-capillary regime d_1 follows:

$$\frac{d_1}{d_1^{**}} = \left(1 - \omega^{**} \frac{t - t^{**}}{t_{\sigma\mu}^{**}}\right) \tag{3}$$

where $t_{\sigma\mu}^{**} = \mu d_1^{**}/\left(2\sigma\right)$ is the characteristic visco-capillary time and μ the liquid dynamic viscosity. The parameters d_1^{**}, ω^{**} and t^{**} depend on the perturbation wavelength. Here, we intend to reproduce this analysis on experimental visualizations of jets of a low-viscosity but elastic liquid i.e., a low-viscosity viscoelastic liquid, showing significant extensional behavior with the objective of tracking the small-scale dynamic.

Dilute solutions of water-soluble polymers are examples of low-viscosity viscoelastic liquids. Jets of such solutions are encountered in diverse domains of applications: inkjet printing technology [11-12], propulsion industry [13], medicine [14] etc.. Jets and filaments of low-viscosity dilute polymer solutions were investigated by several authors in the literature [15, 16, 17 to cite a few examples]. The main feature of these non-Newtonian flows is the evolution of the jet at late times into beads-on-a-string structures where the drop-regions are connected by thin filaments, disappearing only asymptotically [18]. These structures tend to retard final jet breakup and this delay is described by an elasticity-controlled thinning regime. It is now well established (see for instance [19]) that the time evolution of $D_{min}(t)$ in the elasticity-controlled thinning regime is exponential and writes [20]:

$$\frac{D_{min}(t)}{D_j} = \left(\frac{GD_j}{4\sigma}\right)^{1/3} exp\left(-\frac{t}{3t_r}\right) \quad (4)$$

with t_r the relaxation time of the polymer solution and G the modulus of the dilute solution. If the multi-scale tool can provide a measurement of the dynamics of $D_{\min}(t)$, as it was shown on simulated jets of a Newtonian fluid [9], it will allow us to get a measurement of t_r. This would be of particular interest since measuring the extensional properties of mobile liquids is known to be challenging [5, 21]. We will discuss the corresponding literature in more detail later in the paper.

In the present study, we apply the 2D multi-scale analysis to experimental visualizations of free-falling jets of a low viscous and very dilute polymer solution. From the analysis, we extract two characteristic time-scales, the inverse of the growth rate of the instability and the relaxation time of the polymer solution, for different operating conditions. The article is structured as follows. The 2D multi-scale analysis is detailed in section 2. Section 3 presents the fluids, experimental set-up and operating conditions, as well as the measurement protocol. In section 4, the results and analysis are exposed and a discussion of our results with respect to previous work is proposed. We end the article with a conclusion.

2 2D multi-scale description

The concept of 2D multi-scale description and analysis of free liquid flows is introduced in this section. The presentation is restricted to the elements relevant for the present work. (More details are available in [6-9].) The 2D multi-scale description of a liquid system consists in measuring the cumulative scale distribution of its 2D projection. Inspired from the Euclidean Distance Mapping method to measure fractal dimension [22], the cumulative scale distribution is built from successive erosion operations of the 2D projection for a scale d ranging from 0 to infinity. The erosion operation at scale d consists in removing a strip of width $d/2$ around the whole system. The cumulative scale distribution $E_2(d)$ is the measurement of the relative amount of system surface area removed after the erosion operation at scale d. If S_T designates the surface area of the system 2D projection and $S(d)$ the remaining surface area after the erosion at scale d, $E_2(d)$ writes:

$$E_2(d) = \frac{S_T - S(d)}{S_T} \tag{5}$$

For $d = 0$, $S(d) = S_T$ and $E_2(0) = 0$. For a sufficiently large scale, the erosion operation removes all the system and the remaining surface area $S(d) = 0$: therefore $E_2(d) = 1$. For intermediate scales, $S(d)$ keeps decreasing or remains constant while d increases. Therefore, $E_2(d)$ is a cumulative and the smallest scale for which $E_2(d) = 1$ is the maximum scale d_{max} of the system as mentioned in the Introduction section. The first derivative of $E_2(d)$ in the space scale introduces the scale distribution $e_2(d)$:

$$e_2(d) = \frac{\mathrm{d}E_2(d)}{\mathrm{d}d} \tag{6}$$

The dimension of $e_2(d)$ is the inverse of a length. This function is the ratio of the perimeter of the eroded system at scale d on twice the surface-area S_T. The functions $E_2(d)$ and $e_2(d)$ depend on the shape of the system but they are not a measurement of this shape since systems with different shapes may report identical scale distributions.

For simple objects, the distribution $e_2(d)$ can be analytically established. This is the case for a sphere and for a cylinder with a high aspect ratio. These objects are particularly relevant in the context of liquid atomization during which drops and ligaments are often encountered structures. The 2D projections of these objects are a circle and a rectangle, respectively, and their scale distribution $e_2(d)$ writes:

Sphere of diameter D_s:

$$\begin{cases} e_2(d) = \dfrac{2}{D_s}\left(1 - \dfrac{d}{D_s}\right) & \text{for } d \le D_s \\ e_2(d) = 0 & \text{for } D_s < d \end{cases} \tag{7}$$

Cylinder of diameter D_c and length L with $L/D_c >> 1$:

$$\begin{cases} e_2(d) = \dfrac{1}{D_c} & \text{for } d \le D_c \\ e_2(d) = 0 & \text{for } D_c < d \end{cases} \tag{8}$$

The surface-based scale distribution of a sphere depends linearly on the scale (Eq. (7)). On the other hand, the surface-based scale distribution of a cylinder is independent of the scale (Eq. (8)). Therefore, the scale distribution easily discriminates liquid ligaments from drops.

When the shape of the liquid system varies with time, the scale distribution becomes a function of the scale and of the time and writes $e_2(d,t)$. It is important to mention here that the temporal variation of $e_2(d,t)$ might result from the variation of the perimeter of the eroded system, the variation of the surface-area, or the variation of both of them. For dimension reason, it is convenient to consider the inverse of $e_2(d,t)$ introducing the scale-diameter $D(d,t)$ [7]:

$$D(d,t) = \frac{1}{e_2(d,t)} \tag{9}$$

The scale-diameter has the dimension of a length. For a cylindrical ligament, we see from Eq. (8) that the scale diameter is scale independent and is always equal to the ligament diameter, i.e., $D(d,t) = D_c(t)$. Inversely, for a non ligamentary structure, the scale diameter is scale dependent.

As an illustration, these notions are applied to a synthetic beads-on-a-string system made of a sphere of diameter D_{s0} and of a cylinder of diameter D_{c0} and length L. Shown in Fig. 1, this system is assumed of constant volume during time. The cylinder is subjected to a contraction motion characterized by a constant length and an exponential decrease of its diameter as:

$$D_c(t) = D_{c0}\exp(-\alpha t) \tag{10}$$

where α is the growth rate. The decrease of volume of the cylinder is compensated by the equivalent increase of volume of the sphere. The sphere diameter increases therefore as:

$$D_s(t) = \left[{D_{s0}}^3 + \frac{3L}{2}\left({D_{c0}}^2 - D_c(t)^2 \right) \right]^{1/3} \tag{11}$$

During the process, the 2D-projection system surface area (surface area of the drawing shown in Fig. 1) varies as:

$$S_T(t) = D_c(t)L + \frac{\pi D_s(t)^2}{4} \tag{12}$$

The process lasts until the volume of the sphere equals the all volume, i.e., when $D_c(t)$ approaches zero. Introducing this condition into Eq. (11) leads to the final sphere diameter D_{sfin}:

$$D_{sfin} = \left({D_{s0}}^3 + \frac{3L{D_{c0}}^2}{2} \right)^{1/3} \tag{13}$$

The scale-diameter $D(d,t)$ is calculated from Eqs. (7-9, 10-12). For $D_s < D_{sfin}$, it comes:

$$\begin{cases} d < D_c(t) & D(d,t) = \dfrac{S_T(t)}{L + \dfrac{\pi}{2}(D_s(t) - d)} \\ D_c(t) < d < D_s(t) & D(d,t) = \dfrac{2S_T(t)}{\pi(D_s(t) - d)} \end{cases} \tag{14}$$

Note that the scale-diameter is never defined for scales higher than $D_s(t)$ since the corresponding $e_2(d,t)$ is equal to 0. A calculation has been performed with the following set of parameters: D_{s0} = 500 µm, D_{c0} = 100 µm, L = 5 mm, α = 0.2 $(\text{ms})^{-1}$. For this case, Eq. (13) gives D_{sfin} = 584.8 µm. The top graph of Fig. 2 displays the temporal evolution of the scale-diameter for d ranging from 0 to 90 µm. Since the synthetic system considered here is 'discontinuous', i.e., there is no physical connection between the cylinder and the sphere, the function $D(d,t)$ is not continuous at the time for which $d = D_c(t)$. Of course, this will not be the case for actual systems that are continuous. Thus, for the present synthetic example, the $D(d,t)$ curves are drawn continuous in the top graph of Fig. 2. Figure 2 also shows the temporal evolution of the diameter $D_c(t)$ of the cylinder.

We clearly see in Fig. 2 that the scale diameter $D(d,t)$ is rather scale independent provided that $d < D_c(t)$. This scale independence is related to a rather high value of the parameter L (see Eq. (14)). If $D_c(t)$ decreases, the width of the interval of small scales less than $D_c(t)$ decreases accordingly and for any scale becoming higher than $D_c(t)$, $D(d,t)$ suddenly increases as shown in the top graph of Fig. 2. In other words, the detection of the cylinder-diameter decrease can be recognized by identifying the scale d leaving the small-scale interval as time goes.

The specific scale delimiting the small-scale interval is precisely the scale d_1 mentioned in the Introduction section. In the synthetic situation represented in Fig. 2, $d_1(t)$ is equal to the cylindrical diameter $D_c(t)$: $d_1(t)$ is the scale for which $D(d,t)$ stops decreasing and increases sharply (see for instance the behavior of $D(d,t)$ at $t = 1$ ms for $d = 80$ µm or at $t = 2.4$ ms for $d = 60$ µm). For an actual system, the variation of $D(d,t)$ is not that sharp and its continuous time-derivative goes through zero. Therefore, the characteristic scale $d_1(t)$ is defined as the smallest scale for which the time-derivative of the scale diameter is equal to zero. In the case of the beads-on-a-string deformation process, this scale reports the same dynamic as the diameter of the string.

3 Test fluids, experimental set-up and measurements

3.1 Test fluids

The low-viscosity viscoelastic fluid is a polymer solution containing 5 part per million (ppm) of Poly(ethylene oxide) (PEO) dissolved into a solvent. The average molar mass of the PEO is $M_v = 8\ 10^3$ kg/mol, as stated by the manufacturer (Sigma-Aldrich), and the solvent is an aqueous mixture containing 5% in mass of isopropyl alcohol. The density ρ, the shear viscosity μ and the surface tension σ of the solution were measured at room temperature: $\rho = 989$ kg/m^3, $\mu = 1.34$ mPa.s, $\sigma = 48.9$ mN/m. These values are very similar to those obtained for the solvent ($\rho_s = 989$ kg/m^3, $\mu_s = 1.24$ mPa.s, $\sigma_s = 49.3$ mN/m). To measure the elongational properties of viscoelastic solutions it is common to use a Capillary Breakup Extensional Rheometer (CaBER) [23, 24]. This technique relies on the filament thinning in a stretched liquid bridge. But the CABER is not appropriate to characterize the viscoelastic solution used in the present work due to its mobile nature (see [5] for more details). For now, its relaxation time t_r is estimated from the Zimm model in a good solvent [25], $t_r \sim \mu_s[\mu]M_v/(\rho RT)$, which is commonly used to describe dilute polymer solutions as the one studied and characterized here by a low value of c/c*. T is the temperature of the solution, R the gas constant, $[\mu]$ the intrinsic viscosity of the PEO in the solvent, c the concentration of the solution and c* the overlap concentration for polymer coils, calculated as the inverse of $[\mu]$. At T = 20°C, $[\mu]$ was measured by rotational rheometry ($[\mu] = 2.9 \times 10^{-3}$ ppm^{-1}) from which the values $c/c^* \sim 0.015$ and $t_r \sim 12$ ms were deduced.

3.2 Experimental set-up

The free falling jet experimental set-up is drawn in Fig. 3. It includes three major parts: the injector, the liquid pressure-controlled system and the visualization technique.

The injector is a cylindrical body ended with a cylindrical discharge orifice. It is oriented in the vertical direction $(0, z)$ (see Fig. 3). The liquid feeds in the cylindrical body with an imposed pressure and then discharges through the orifice as a free falling liquid jet, i.e., a vertical jet with no imposed perturbation. The length and diameter of the injector body are equal to 85 mm and 5 mm, respectively. The cylindrical discharge orifice has a diameter $D_{or} = 200\ \mu$m and a length $L_{or} = 300\ \mu$m. The liquid pressure-controlled system consists of an air pressure tank with flexible pipes. The pressure is manually adjusted with an expansion valve and is controlled with an air pressure sensor located ahead of the injector. The injector is mounted on a computer-controlled three-axis displacement system. In particular, the vertical adjustment allows us to select different positions along the $(0, z)$ axis from the orifice exit. The jet production system operates in a wide and open chamber equipped with windows whose role is to protect the liquid jet from any external perturbations.

Snapshots of the liquid jet issuing from the injector are recorded by using a shadowgraph optical method. The light source, the object and the image sensor are aligned and fixed on an optical bench. The light source is a HSPS NANOLITE KL-L whose flash duration is of the order of 20 ns. The receiver is a sCMOS pco.edge 5.5 USB sensor (2560 x 2160 pixels) with an integrated shutter. The optical recording system, i.e. light source, image sensor and acquisition, is synchronized by a TTL signal. The field covered by the image is 6.56 mm (height) x 5.54 mm (width). The corresponding spatial resolution is equal to 2.56 µm/pixel. For every operating condition, this optical arrangement ensures frozen liquid flow images. To follow the jet evolution from the nozzle exit down to the fragmentation region, the injector is vertically shifted using the three-axis displacement system. Considering the physical height of the visualized field

(6.56 mm), the vertical shift was taken equal to 6 mm. At each vertical position, 204 images were taken at a 10 Hz frequency. The proximity of this frequency with the one of the jet capillary instability which, according to linear stability theory [1] is equal to 2.4 Hz, is not penalizing for two reasons. First, the liquid system for free-falling jets implies a certain variability in space and time and avoids any unfavorable locking between the behavior and the observation. Second, the images are fully uncorrelated in time since during 0.1 s the jets travel 190 mm at least which is much higher than the image height.

The experimental runs were performed under atmospheric ambient pressure and temperature (between 19°C and 21°C). The injection pressure ranged from 0.05 bar to 1 bar, corresponding to a mean jet velocity V_q ranging from 2 to 10 m/s. This velocity was obtained by dividing the volume flow rate by the section area $\pi D_j^2/4$, where D_j is the mean jet diameter measured close to the orifice exit before any perturbation becomes visible (see Table 1). The experiments were performed in two groups: 1 – reproducibility experiments; 2 - jet velocity dependency experiments. In group 1, the injection pressure was adjusted to obtain a velocity V_q around 8 m/s. This single experiment was repeated four times in a row. They are identified Run #1 to #4 in the following. In group 2, seven experiments with a varying velocity V_q were performed and are identified Run #5 to #11 in the following (see Table 1). In every case, the liquid jet was never turned off during the experiments. The Reynolds number $Re = \rho V_q D_j/(2\mu)$, Ohnesorge number $Oh = \mu/\sqrt{\rho\sigma D_j/2}$, Deborah number $De = \sqrt{8\sigma t_r^2/\left(\rho D_j^3\right)}$, liquid Weber number $We = \rho V_q^2 D_j/(2\sigma)$ and Froude number $Fr = V_q/\sqrt{gL_{BU}}$ (where L_{BU} is the average breakup length and g the gravitational acceleration) corresponding to the operating conditions explored during this work are: $1.5 \times 10^2 \leq Re \leq 7.0 \times 10^2$, $1.9 \times 10^{-2} \leq Oh \leq 2.0 \times 10^{-2}$, $75 \leq De \leq 95$, $7.7 \leq We \leq 2.0 \times 10^2$ and $3.7 \leq Fr \leq 13$. These numbers say that the present jets are laminar, weakly viscous, elastic and sometimes sensitive to the gravitational acceleration.

3.3 Measurements

The images taken at several z positions can be used to reconstruct the entire jet from the nozzle exit down to the breakup region. An example of this is shown in Fig. 4 for the polymer solution at 8 m/s (we remind here that the image height is 6.56 mm and that the injection is performed vertically). We see in Fig. 4 that the jet maintains a rather cylindrical and unperturbed shape along 17 mm. At this position, a clear and sinusoidal perturbation becomes visible. This perturbation grows in amplitude with the downstream position keeping its sinusoidal shape down to 25 mm. After this position, the deformation process continues but the shape of the perturbation significantly varies leading to the expected beads-on-a-string pattern at 30 mm. This pattern remains visible until breakup occurs at 43 mm. In this work, the multi-scale tool introduced in Section 2 is used to describe this process.

The multi-scale description starts with the measurement of the cumulative scale distribution from the analysis of the experimental images. This image analyzing stage can be summarized in four steps illustrated in Fig. 5. First, the raw images (Fig. 5-a) are normalized (Fig. 5-b) in order to produce images with identical and constant background level. Second, the normalized images are binarized (Fig. 5-c). A single threshold is determined from the gray-level histogram to segregate the liquid pixel from the background pixel. The resulting images have two gray levels only; black for the liquid and white for the background. Third, a correction is applied to remove the white dots or zones that may remain on the axis of the liquid jet (Fig. 5-d). Resulting from non-deviated light, these white stains reveal the laminar and smooth nature of the jet. Fourth, the Euclidian Distance Mapping is applied (Fig. 5-e). This step consists in attributing to each black (liquid) pixel a gray level equal to the distance (in pixels) of the nearest interface boundary.

The cumulative scale-distribution is obtained from the count of pixels according to these gray-levels. This measurement is local, i.e., the count is performed on a portion of the jet delimited

by a rectangular analyzing window of height H_w (see Fig. 5-e). This operation is repeated on the 204 iso-z images and an averaged cumulative distribution $E_2(d,t)$ is calculated that is attributed to the analyzing-window middle-line position z and then to the equivalent time t defined by:

$$t = \frac{\sqrt{V_q^{\,2} + 2gz} - V_q}{g} \tag{15}$$

In particular, the average breakup time t_{BU} is obtained for $z = L_{\mathrm{BU}}$. When $V_q^2 >> 2gz$ ($Fr >> 1$), Eq. (15) simplifies as $t = z/V_q$. The temporal evolution of the cumulative distribution is then obtained by sliding the Analyzing Window from the top to the bottom of the image with a spatial shift of ΔH_w. The image analyzing procedure has been conducted with the free ImageJ software. It requires values for the parameters H_w and ΔH_w.

The choice of the height of the analyzing window H_w is a compromise between the necessity of having a local information and a statistical information. If H_w is small the information is very local but a high number of images is required to ensure a good statistic. If H_w is large, less images are needed but the local aspect of the measurement is lost which manifests by a strong dependence between $E_2(d,t)$ and H_w. The adopted protocol to choose H_w is the one reported in [9]: $E_2(d,t)$ is measured for a decreasing H_w and the highest H_w from which $E_2(d,t)$ stops varying is selected. The application of this protocol leads to H_w = 1.0 mm. This parameter is of the order of magnitude of the beads-on-a-string pattern (see Figure 4).

The parameter ΔH_w is the shift of the analyzing window: it controls the temporal resolution ($= V_q/\Delta H_w$) which should be adjusted to allow a good following of the temporal variations. If the temporal resolution is too high, the variations of the system might be too small to be accurately measured. Subsequently, any temporal derivative might be pretty incorrect. If the

temporal resolution is too small, the variations of the system might be too high to report an accurate perception of the dynamic. The selection we made in the paper (ΔH_w = 1.0 mm) offers a good compromise between these two extreme situations. Both parameters H_w and ΔH_w have been kept constant for all positions and velocities.

Once the cumulative distribution $E_2(d,t)$ are obtained, they are corrected from the inaccuracy of the Euclidian Distance Map tool in the small scales and smoothed in the scale and time spaces. Then, the scale distribution $e_2(d,t)$ and the scale diameter $D(d,t)$ are calculated (Eqs. (6) and (9) respectively) and the characteristic scales d_{max} and d_1 are determined with the free software Scilab. The characteristic scales d_{max} and d_1 have been introduced in Section 2. They are determined as follows. The maximum scale d_{max} is taken as the smallest scale for which $E_2(d,t) \geq 0.995$ instead of $E_2(d,t) = 1$. The threshold 0.995 is the highest value for which an exponential increase in time is ensured for d_{max} for all working conditions. It excluded unphysical and overestimated value of d_{max} when they exist. It has been checked that in the absence of these overestimated d_{max}, the threshold 0.995 brings the same dynamics as the theoretical threshold 1. The scale d_1 is determined as the smallest scale satisfying:

$$\frac{\mathrm{d}D(d,t)}{\mathrm{d}t} = 0 \tag{16}$$

The accuracy of the determination of these two scales is limited by the image spatial resolution. The effect of this is the existence of a non-reliability region for every result involving these scales.

4 Results and Discussion

The typical temporal evolution of the scale diameters $D(d,t)$ for the jet of the polymer solution is shown in Fig. 6-a for several scales (Group 1, Run #1, see Table 1). As said above, this jet is subject to a beads-on-a-string deformation process (see the image incrusted in the figure). By way of a comparison, the temporal evolution of the scale diameters $D(d,t)$ for a solvent jet (with no polymer) is shown in Fig. 6-b for several scales (V_q = 2 m/s, $D_j = D_{or}$ = 300 µm). For this case also, an image showing the liquid jet deformation is incrusted in the figure. Because of the absence of polymer, no beads-on-a-string pattern is observed. Instead, a classical Newtonian liquid behavior takes place. Figure 6 shows that the scale diameter $D(d,t)$ is very sensitive to the jet deformation and breakup process. For both liquids, the scale diameter is independent of the scale at initial times and becomes scale-dependent as time increases. The main difference between the two liquids is the time duration of this scale-dependency development: it starts at t/t_{BU} = 0.2 and 0.75 for the polymer solution and the solvent solution, respectively. This difference is related to the characteristic time of the small structure life-time. As explained in Section 2 (see Fig. 2), the scale-dependency development seen in Fig. 6-a is representative of the thinning ligament dynamics.

Figure 7 shows the temporal evolution of d_{max} for Run #1. The gray zone in the figure corresponds to the non-reliability region. Disregarding the first values falling in the non-reliability region, we see that d_{max} monotonously increases with time. This behavior is expected since this scale is equal to the jet crest diameter. Two zones of increase are visible. First (for $0.4 < t/t_{BU} < 0.55$) the temporal increase is exponential as the one expressed by Eq. (1). This behavior corresponds to the capillary instability as described by the linear stability theory. The growth rate of the instability can be obtained from the slope of the linear behavior marked in

Fig. 7 by a dash line. Second (for $0.55 < t/t_{BU} < 1$) the d_{max} increase considerably slows down. Considering that for Run #1 $t_{BU} = 5.4$ ms, we can evaluate that the transition between the two zones occurs at around $z = 25$ mm. Figure 4 shows that this position is the one where the jet rearranges as a beads-on-a-string configuration. The temporal evolution of d_{max} obtained for the four Runs of Group 1 (see Table 1) are compared to each other in the insert figure. As far as the dynamic of d_{max} is concerned, we see that the experimental protocol reports an excellent reproducibility.

The scale d_1 is the one for which the temporal derivative of the scale diameter is equal to zero (see section 2). Figure 8 shows the temporal evolution of this scale for the experimental Run #1 under a dimensionless form. The non-reliability region is indicated in gray. For $0.5 < t/t_{BU} < 0.9$, we see that d_1 exponentially decreases in time. The corresponding growth rate is expected to be related to the relaxation time t_r as expressed by Eq. (4). For higher times, the points deviate from the exponential behavior. Due to finite extensibility of the polymer molecules, a physical argument often used in the literature to model viscoelastic behaviors (see for instance the work of Entov & Hinch [26]), the elastic response is limited. The viscous response continues to grow, the only one balancing the capillary thinning of the filament. This last stage is thus the expected visco-capillary regime. However, there are too few points to allow for its quantitative characterization. The plot incrusted in Fig. 8 compares the results for the four runs. The behaviors in the exponential stage are clearly parallel demonstrating the reproducibility of the experimental protocol to extract the relaxation time from the decrease of the scale d_1 (the value found for the four experimental runs of Fig. 8 is 0.48 ms).

In the present jet regimes (Rayleigh regime) the growth rate of the linear instability is supposed to be independent of the mean jet velocity. Furthermore, the relaxation time is an intrinsic property of the solution and should not depend on the mean jet velocity as well. Group 2

experimental runs would show us whether the characteristic times extracted from d_{max} and d_1 fulfill this non-dependency.

The experimental protocol and analysis detailed above was scrupulously reproduced for the seven experimental runs of Group 2 (see Table 1). For each case, the wavenumber k of the initial perturbation was determined from the estimation of the wavelength λ ($k= 2\pi/\lambda$) identified on the images as shown in Fig. 4. Furthermore the linear growth rate ω of the perturbation was also determined from the exponential increase of the scale d_{max} as shown in Fig. 7. For all operating conditions, Fig. 9 shows the initial perturbation wavenumber and growth rate as a function of the root square of the Weber number. Experimental data points are found in good agreement with the predictions of linear stability theory for the fastest growing mode and the maximum growth rate (indicated by the horizontal lines in Fig. 4.6). The theoretical values are obtained from the model of Brenn et al. [27] for a non-Newtonian fluid using the Ohnesorge of the PEO solution, the Deborah number calculated with the Zimm relaxation time and the time ratio taken as the viscosity ratio of the solvent viscosity to the polymer solution one. These values are very similar to the ones predicted by Rayleigh $kD_j/2 = 0.69$ and $\omega t_\sigma = 0.34$ since the polymer solution studied here is a low-viscosity solution. We note also that the measured growth rates are never above the Rayleigh's theoretical limit. The good agreement between experiment and theory on Fig. 9 demonstrates that the observed perturbation is the optimum one, confirming the free nature of the liquid jets.

For all operating conditions, the elasto-capillary regime of the d_1 scale was identified and the relaxation time t_r was evaluated from the slope in this regime according to Eq. (4). The results are plotted in Fig. 10 as a function of the root square of the Weber number. This figure clearly evidences a dependency between the relaxation time and the Weber number. However, two points must be mentioned. First, the relaxation times found for the four runs of Group 1 are very close to each other. This validates the reproducibility of the experimental procedure.

Second, whereas the relaxation time depends on the Weber number, an asymptotic value is reached as the Weber number increases. This asymptote is recognized by the mathematical fit reproduced in the figure and the corresponding asymptotic relaxation time is t_r = 0.44 ms.

The idea of using a viscoelastic jet behavior to determine the relaxation time of a polymer solution is not new. It defines a method for elongational rheometry whose proof-of-concept was originally demonstrated by Schümmer & Tebel [28-30] and that was recently developed by Keshavarz et al. [5].

Schümmer & Tebel [28-30] reported the dependency of the relaxation time to jet operating conditions. Forced jet experiments with the same polymer solution but different operating conditions – amplitude and frequency of nozzle disturbance and jet velocity – were conducted. For the range of parameters explored, it was shown that an increase in disturbance amplitude or frequency but a decrease in mean jet velocity causes a decrease of the relaxation time (see for instance Fig. 14 in [30] for more details on the domain of jet operation). According to these authors, it should be possible to identify suitable operating conditions for which a unique relaxation time can be obtained. So far, the existence of this suitable operating domain has not been fully demonstrated, limiting the use of the jet behavior to probe elongational properties of fluids.

Recently, there has been a resurgence of interest for the jet elongational rheometer. One reason is that this technique allows to address the well-known challenge of elongational rheology for very dilute polymer solutions, as proved and discussed in great details in the recent work of Keshavarz et al. [5]. In this quantitative investigation on atomization of viscoelastic liquid jets, the authors introduced the use of the Rayleigh Ohnesorge Jetting Extensional Rheometry (ROJER) to obtain precise measurements of elongational properties for very dilute polymer solutions. The technique relies on the filament thinning in a vibrating jet, based on the original

ideas from Schümmer & Tebel [28-30], and can be seen as a “flying CABER”. In that work, it was found that for fixed disturbance amplitude and frequency the value of the relaxation time did not depend on the jet velocity.

For the present experiments, only the injection pressure is imposed. Note that a change in the injection pressure causes a change both in the mean jet velocity and the mean jet diameter, which are used to calculate the Weber number. As can be seen in Table 1, the jet at the exit of the orifice experiences an expansion or a contraction depending on the injection pressure, a phenomenon that is already known for Newtonian fluids [see for example [31]] and that is expected to be modified here by the die-swell effect of the polymer solution [32]. On the other hand, the disturbance amplitude and frequency are freely selected by the physical system. Based on the results of Fig. 9, we can reasonably assume that the experiments are performed at a constant disturbance frequency, the most unstable one. Although the disturbance amplitude has not been measured, its dependency with the Weber number is evidenced by the luminous line on the axis of the liquid jet near the injector. Figure 11 reports a series of images taken at the orifice exit for four different experiments of Group 2. We observe that the sinuosity of the luminous central line increases with the Weber number. A close examination of image series reveals that this sinuosity is constant with time and therefore highlights a steady-state deformation of the jet, which generates a larger initial perturbation amplitude. This means that, in our free jet conditions, an increase in Weber number causes an increase in initial disturbance amplitude. On the other hand, Fig. 10 shows that a Weber number increase causes a decrease of the relaxation time. Considering Schümmer & Tebel’s findings [28-30], these elements tend to demonstrate that the effect of disturbance amplitude is dominant over the one of jet velocity in the present work: the decrease of relaxation time with the Weber number due to a decrease of mean jet velocity is due to an increase of the initial disturbance amplitude.

It is important to emphasize that the high values of the relaxation times are obtained for the low Weber numbers experiments (Runs # 5-7, $We = 8, 25, 43$ see Table 1). One may wonder whether the system is not close to the dripping-jetting transition for which a gobbling effect may modify the characteristic time of the filament thinning while preserving its exponential behavior [33] or not. The critical Weber number (see equation 3.1 and 3.2 in [33]) was estimated close to 2, confirming that our jet experiments are strictly above the fully-developed gobbling regime. Assuming the presence of residual gobbling gives us a relaxation time 3/2 greater than the one measured here, which makes the difference between the values at low and high Weber numbers even larger. Thus, the gobbling effect can not explain the high values of the relaxation time obtained in the low Weber number experiments.

The present experiments show also that for sufficient large Weber numbers, the relaxation time becomes quasi-independent of the Weber number, in agreement with the conclusion of Schümmer & Tebel [28-30] speaking for the existence of a suitable operating domain. The results of Keshavarzk et al. [5] that reported no velocity effect, seems to prove the existence of this domain. Yet, these results require to be confirmed by a series of additional experiments, in order to better understand the effect of the perturbation amplitude on the relaxation time in both free and forced jet experiments. A more detailed study is thus needed to precise the domain of operation where a unique relaxation time can be achieved with a jet elongational rheometer.

5 Conclusion

The 2D multi-scale analyzing tool developed to diagnose liquid atomization processes has been applied on images of free-falling jets of a low viscous and very dilute polymer solution showing beads-on-a-string structures. Performing a global description of the liquid jet, the multi-scale approach allows identifying and isolating the dynamics at different scales involved in the jet deformation process. Because of the viscoelastic nature of the liquid, the present jet deforms in two steps; first a sinusoidal perturbation manifests and grows in amplitude, and second this sinusoidal perturbation transforms as a beads-on-a-string structure whose evolution involves the thinning of the string until breakup occurs. The free-falling characteristic of the jet has been proven by the fact that, for every tested liquid jet velocity, the initial perturbation wavelength exhibits the value of the optimum wave predicted by the linear stability theory. The multi-scale analysis concentrates on two scales: the maximum scale d_{max} and the scale d_1 whose dynamic follows the one of the small structure. In the first jet deformation step, d_{max} exponentially increases with time with a growth rate always equal to the linear theory prediction. This again demonstrates the free-falling nature of the jet. In the second jet deformation step, the dynamic of the scale d_1 corresponds to the one of the filament between the beads. This dynamic is found to follow an elasto-capillary regime from which the characteristic relaxation time can be determined. The reproducibility of this technique to determine this time was demonstrated to be excellent. When the jet velocity increases, it is found that the relaxation time decreases and seems to converge towards an asymptotic value. Based on previous works of the literature, this behavior has been identified in the present experiments to result from the increase of the initial amplitude of the perturbation with the jet velocity. This suggests performing further experiments in order to identify operating conditions ensuring the determination of a constant relaxation time independent of the operating conditions. Since high initial amplitude

perturbation has to be privileged, using complex geometry nozzles might constitute an interesting suggestion.

This work shows that the multi-scale approach constitutes an interesting and complementary alternative to the currently used techniques to probe the extensional properties of a visco-elastic solution. This technique has advantages. Since it is based on a global description, it is not subject to a spatial accuracy required by any local technique. Furthermore, no specific condition regarding the injection conditions is required. The multi-scale description can be applied in any situation, whatever the shape of the system. In particular, it would be able to identify and quantify elasto-capillary mechanisms in any situations including complex atomization scenario. Finally, it is also important to mention that, with one measurement, this approach provides all the dynamics involved in the evolution of an atomizing liquid system. The completeness of such information has not been fully exploited so far.

6 Acknowlegments

The authors acknowledge the financial support from the French National Research Agency (ANR) through the program Investissements d'Avenir (ANR-10 LABX-09-01), LABEX EMC3. The authors would like also to thank Prof. Günter Brenn from Graz University of Technology for fruitful discussions.

References

[1] L. Rayleigh, On the Instability of Jets, Proc. Lond. Math. Soc. 10 (1979) 4-13.

[2] S.Chandrasekhar Hydrodynamic and Hydromagnetic Stability, Oxford University Press, (1961)

[3] J. Eggers, E. Villermaux, Physics of liquid jets, Rep. Prog. Phys. 71 (2008) 036601.

[4] C. Clasen, J. Bico, V. Entov, G.H. McKinley, Journal of Fluid Mechanics 636 (2009) 5-40

[5] B. Keshavarz, V. Sharma, E.C. Houze, M.R. Koerner, J. R. Moore, P. M. Cotts, P. Threlfall Holmes, G.H. McKinley, Studying the effects of elongational properties on atomization of weakly viscoelastic solutions using Rayleigh Ohnesorge Jetting Extensional Rheometry (ROJER), J. Non-Newton. Fluid, 222 (2015) 171-189.

[6] C. Dumouchel, S. Grout, Application of the scale entropy diffusion model to describe a liquid atomization process, Int. J. Multiph. Flow 35 (2009) 952-962.

[7] C. Dumouchel, S. Grout, Towards an interpretation of the scale diffusivity in liquid atomization process: An experimental approach, Physica A 390 (2011) 1811-1825.

[8] C. Dumouchel, J.B. Blaisot, E. Bouche, T. Ménard, T.T. Vu, Multi-scale analysis of atomizing liquid ligaments, Int. J. Multiph. Flow 73 (2015) 251-263.

[9] C. Dumouchel, W. Aniszewski, T.T. Vu, T. Ménard, Multi-scale analysis of simulated capillary instability, Int. J. Multiph. Flow 92 (2017) 181-192

[10] C. Clasen, P. M. Phillips, L. Palangetic, J. Vermant, Dispensing of rheologically complex fluids: the map of misery, AIChE J. 58 (2012) 3242-3255.

[11] C. Mcllroy, O. G. Harlen, N. F. Morrison, Modelling the jetting of dilute polymer solutions in drop-on-demand inkjet printing, J. Non-Newton. Fluid, 201 (2013) 17-28

[12] N.F. Morrison, O.G. Harlen, Viscoelasticity in inkjet printing, Rheol Acta, 49 (2010) 619-632

[13] K.K. Chao, C.A. Child, E.A. Grens II, M.C. Williams, Antimisting action of polymeric additives in jet fuels, AIChE J. 30 (1984) 111.

[14] E. Zussman, A.L. Yarin, R.M. Nagler. Age- and Flow-dependency of Salivary Viscoelasticity, J. Dent. Res. 86 (2006) 281.

[15] M. Goldin, J. Yerushalmi, R. Pfeffer, R. Shinnar, Breakup of laminar capillary jet of a viscoelastic fluid, J. Fluid Mech. 38 (1969) 689.

[16] M.S.N. Oliveira, G.H. McKinley, Iterated stretching and multiple beads-on-a-string phenomena in dilute solutions of highly extensible flexible polymers, Phys. Fluids 17 (7) (2005)

[17] P.P. Bhat, S. Appathurai, M.T. Harris, M. Pasquali, G.H. McKinley, O.A. Basaran, Formation of beads-on-a-string structures during breakup of viscoelastic filaments, Nat. Phys. 6 (2010) 625-631.

[18] S. Middleman, "Stability of a viscoelastic jet," Chem. Eng. Sci., vol. 20, no. 12, p. 1037–&, 1965.

[19] M. Stelter, G. Brenn, A.L. Yarin, R.P. Singh, F. Durst, Validation and application of a novel elongation device for polymer solutions, J. Rheol. 44 (2000) 595-616.

[20] D. Vadillo, W. Mathues, C. Clasen, Rheologica Acta 51 (2012), 755-769

[21] Y. Christanti, L.M. Walker, Surface tension driven jet break up of strain-hardening polymer solutions, J. Non-Newt. Fluid Mech. 100 (2001) 9–26.

[22] J. Bérubé, M. Jébrak, High precision boundary fractal analysis for shape characterization, Comput. Geosci. 25 (1999) 1059–1071.

[23] S. Anna, G. McKinley, Elasto-capillary thinning and breakup of model elastic liquids, J. Rheol. 45 (2001) 15.

[24] L. Campo-Deano, C. Clasen, Journal of Non-Newtonian Fluid Mechanics 165 (2010) 1688-1699

[25] M. Doi, S.F. Edwards, The theory of polymer dynamics, Oxford University Press, New-York, 1986.

[26] V. M. Entov and E. J. Hinch, "Effect of a spectrum of relaxation times on the capillary thinning of a filament of elastic liquid," J. Non-Newtonian Fluid Mech., vol. 72, pp. 31–54, 1997.

[27] G. Brenn, Z. B. Liu, and F. Durst, "Linear analysis of the temporal instability of axisymmetrical non-Newtonian liquid jets," Int. J. Multiph. Flow, vol. 26, no. 10, pp. 1621–1644, 2000.

[28] P. Schümmer, K.H. Tebel, The use of controlled jet instability for elongational rheometry, J. Rheol, 26 (1982) 77-78.

[29] P. Schümmer, K.H. Tebel, Design and Operation of the free jet elongational rheometer, Rheol. Acta, 21 (1982) 514-516.

[30] P. Schümmer, K.H. Tebel, A new elongational rheometer for polymer solutions, J. Non-Newton. Fluid, 12 (1983) 331-347.

[31] S. Middleman, J. Gavis, Physics of Fluids 4 (3) (1961) 355-359

[32] R.B. Bird, R.C. Armstrong, O. Hassager, Dynamics of Polymeric Liquids, second ed., vol. 1, John Wiley & Sons, New York, 1987.

[33] C. Clasen, J. Bico, V. Entov, G.H. McKinley, Journal of Fluid Mechanics 636 (2009) 5-40

Figure Captions

Fig. 1: Geometry of the synthetic beads-on-a-string system

Fig. 2: Scale diameter $D(d,t)$ of the synthetic system versus time t for several scales d and the corresponding diameter $D_c(t)$ of the synthetic system cylinder versus time t. The dashed arrows show the correspondence between the cylinder diameter $D_c(t)$ and the scale for which we observe a jump of function $D(d,t)$ at time t.

Fig. 3: Experimental Set-up

Fig. 4: Reconstructed jet. Fluid: polymer solution, $We^{1/2}$ = 12. The double arrow indicates the initial perturbation wavelength identification.

Fig. 5: From the raw image to the Euclidian Distance Map. a) Raw image b) Normalized image c) Binarized image d) Corrected image from the low intensity pixels inside the jet e) Euclidian Distance Map. Fluid: polymer solution. $We^{1/2}$ = 4.3.

Fig. 6: Dimensionless scale-diameter $D(d,t)/D_j$ versus dimensionless time t/t_{BU} for several scales d: a) Fluid: polymer solution, $We^{1/2}$ = 12, b) Fluid: solvent, $We^{1/2}$= 5.0 with $D_j = D_{or}$ =300 μm. Incrusted images show corresponding jet morphology. (t_{BU} is the breakup time)

Fig. 7: Dimensionless maximum scale $d_{max}/D_j - 1$ versus dimensionless time t/t_{BU} for experimental run #1. Fluid: polymer solution. $We^{1/2}$ =12. The dashed line represents the linear stability model. The insert figure shows the results for the four experimental runs of Group 1.

Fig. 8: Dimensionless scale d_1/D_j versus dimensionless time t/t_{BU} for experimental run #1. Fluid: polymer solution. $We^{1/2}$ = 12. The dashed line represents the Elasto-capillary model. The insert figure shows the results for the four experimental runs of Group 1.

Fig. 9: Dimensionless wavenumber $kD_j/2$ and dimensionless growth rate ωt_σ versus the square root of the Weber number $We^{1/2}$. Fluid: polymer solution. The horizontal lines indicate the Brenn theoretical predictions for the most unstable wavenumber and maximum growth rate. Note that the growth rate value of the lower Weber number is not present due to the lack of data points require to determinate it.

Fig. 10: Deborah number $De = t_r/t_\sigma$ versus the square root of the Weber number $We^{1/2}$. Fluid: polymer solution. The dashed curve represents the best fit of the data, searched under the mathematical form: $ae^{bWe^{½}} + c$, with a,b and c being the parameters of the fit.

Fig. 11: Visualization of the amplitude perturbation at the exit of the injector for different Weber number experiments. Injection pressure a) $We^{1/2}$=5.0 b) $We^{1/2}$=8.0 c) $We^{1/2}$=9.8 d) $We^{1/2}$=12.

Tab.1: Identification and operating conditions of the experimental runs. The Weber number *We* is defined in the text (see section 3.2). the text (see section 3.2).

Fig. 1

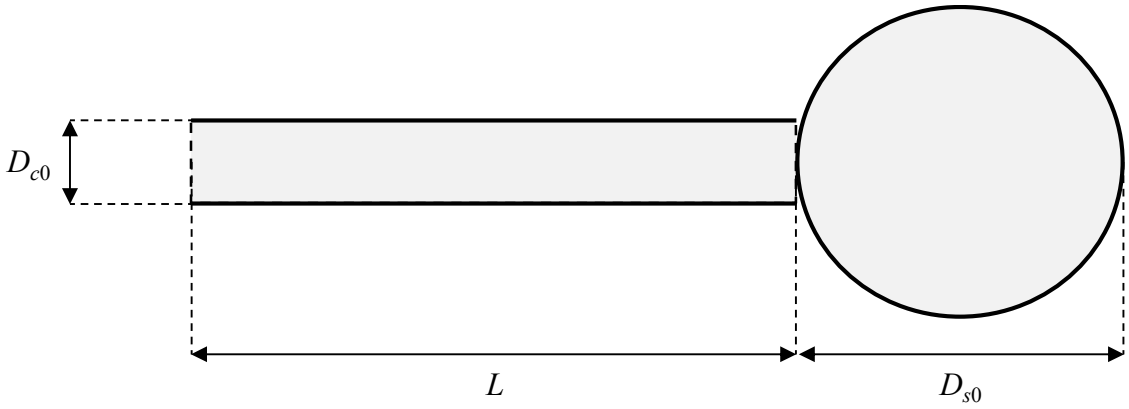

Fig. 2

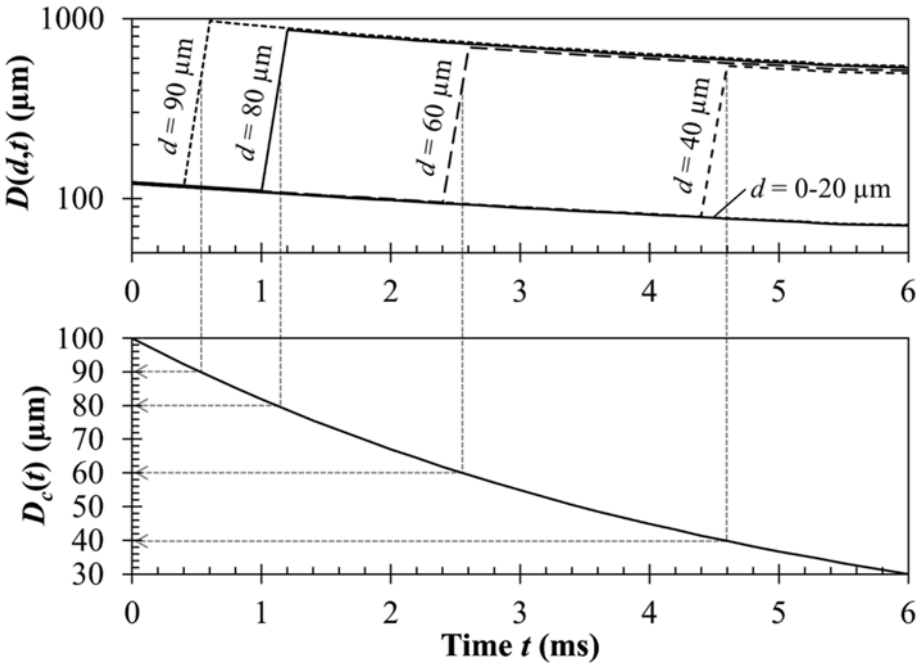
1000
100
D(d,t) (µm)
d = 90 µm
d = 80 µm
d = 60 µm
d = 40 µm
d = 0-20 µm
0
1
2
3
4
5
6
100
90
80
70
60
50
40
30
D_c(t) (µm)
Time t (ms)

Fig. 3

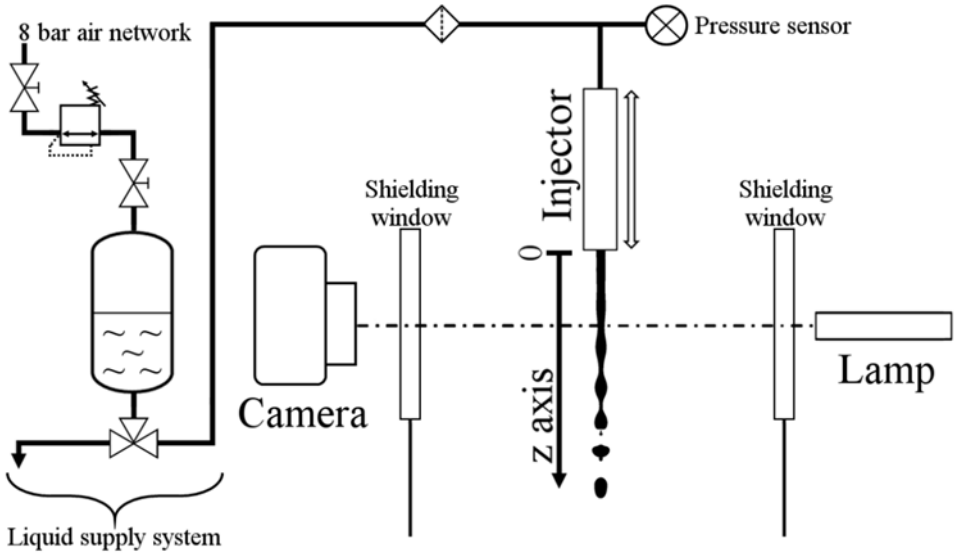
8 bar air network
Pressure sensor
Shielding window
Injector
Shielding window
0
Camera
z axis
Lamp
Liquid supply system

Fig 4

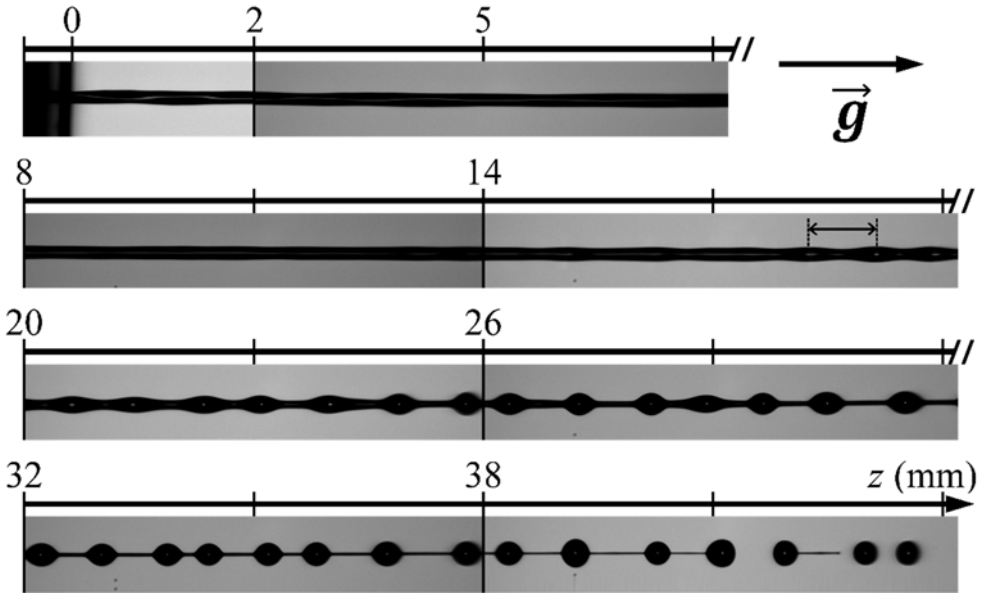

Fig. 5

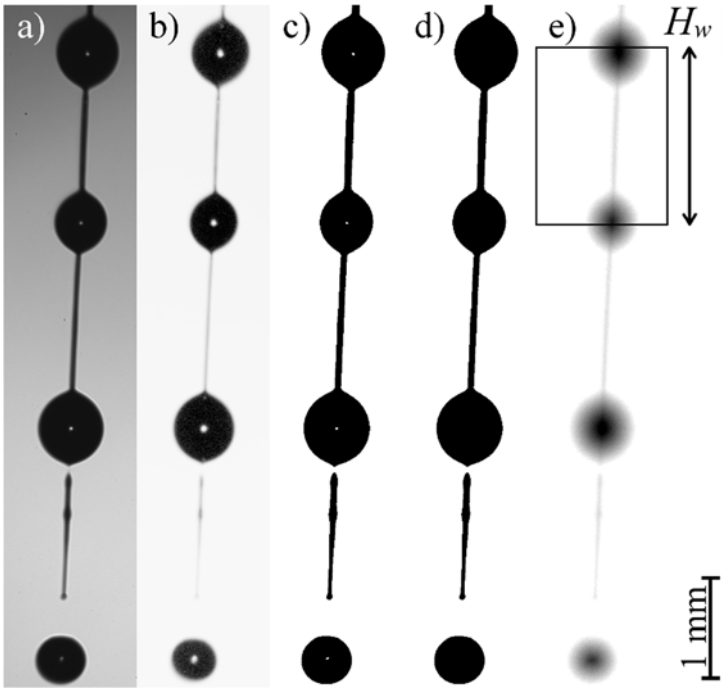

Fig. 6

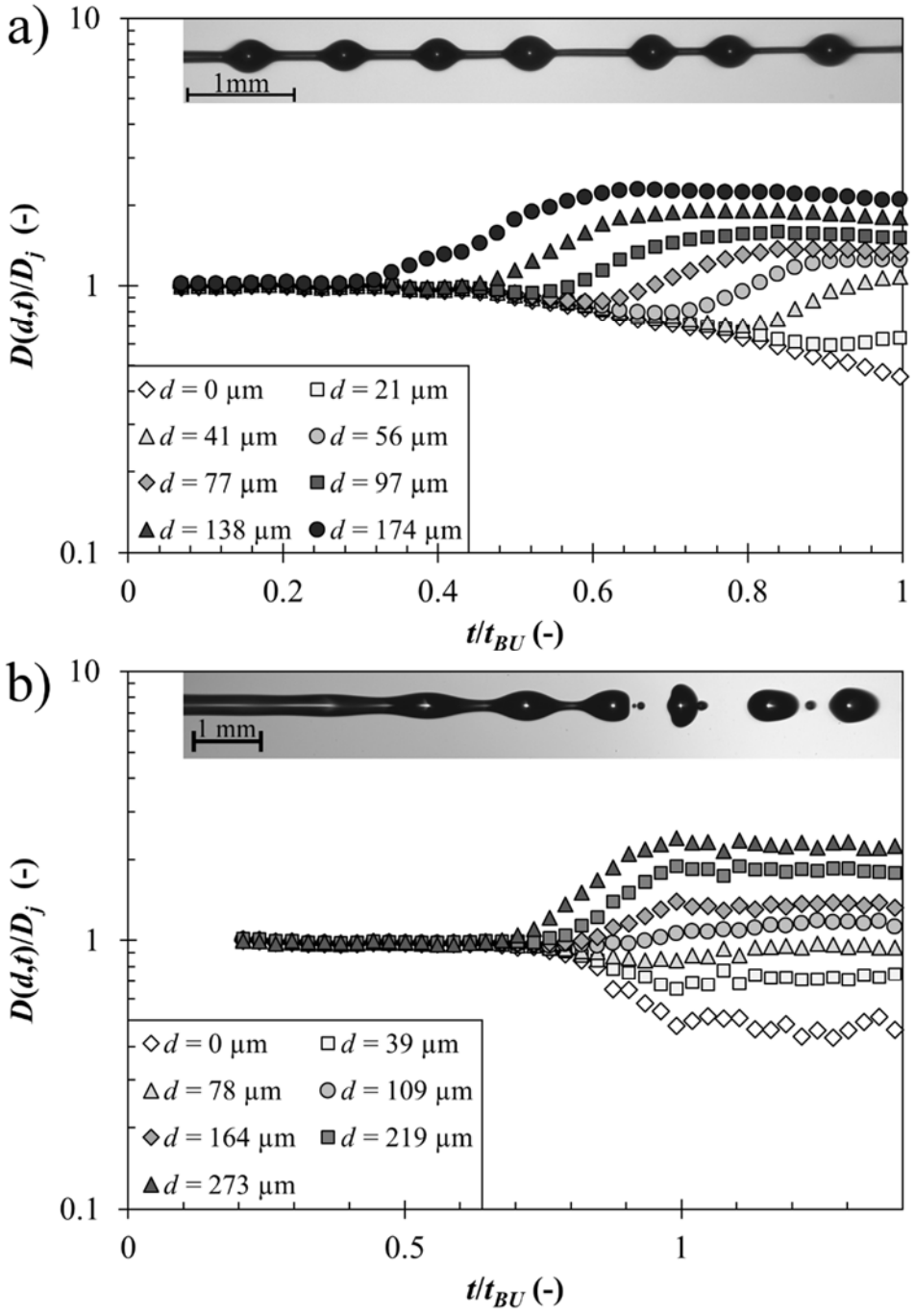
a)
1mm
10
1
0.1
D(d,t)/D_j (-)
d = 0 µm
d = 21 µm
d = 41 µm
d = 56 µm
d = 77 µm
d = 97 µm
d = 138 µm
d = 174 µm
0
0.2
0.4
0.6
0.8
1
t/t_BU (-)
b)
1 mm
10
1
0.1
D(d,t)/D_j (-)
d = 0 µm
d = 39 µm
d = 78 µm
d = 109 µm
d = 164 µm
d = 219 µm
d = 273 µm
0
0.5
1
t/t_BU (-)

Fig. 7

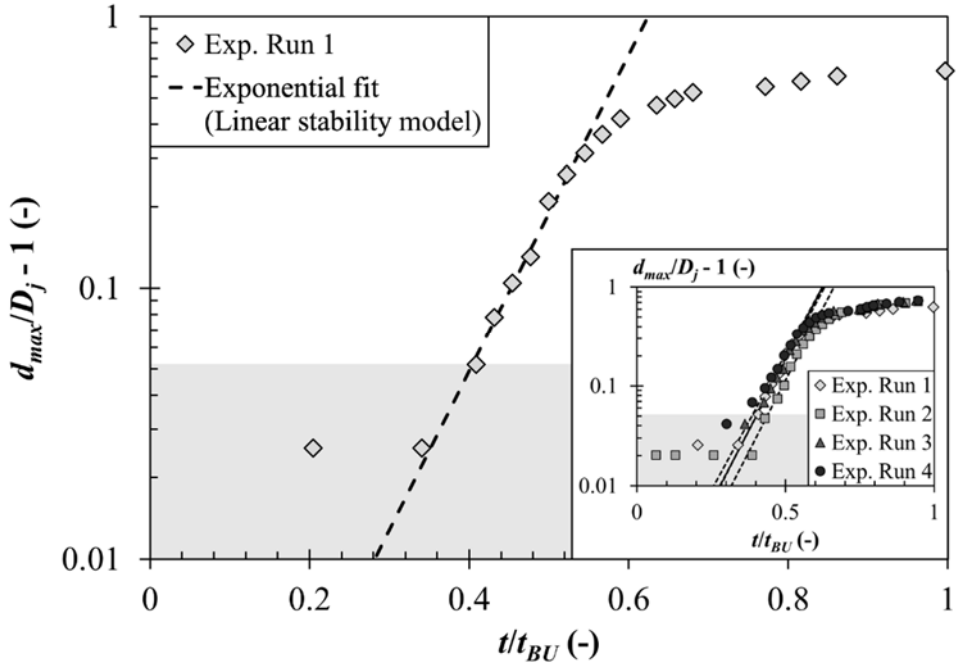
Exp. Run 1
Exponential fit
(Linear stability model)
d_{max}/D_j - 1 (-)
t/t_{BU} (-)
1
0.1
0.01
0
0.2
0.4
0.6
0.8
1
Exp. Run 2
Exp. Run 3
Exp. Run 4
0.5

Fig. 8

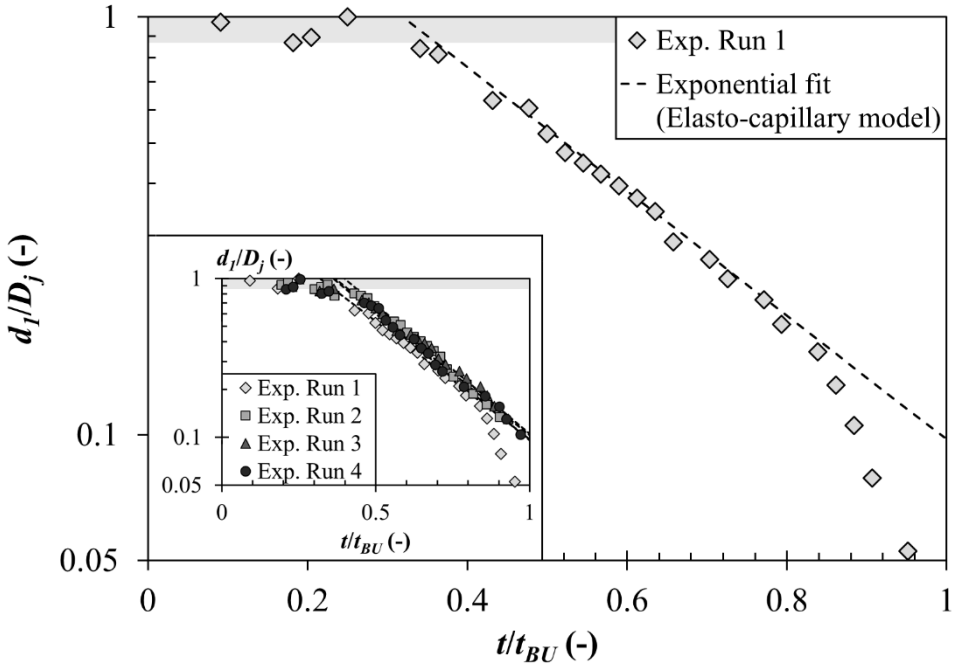
1
0.1
0.05
0
0.2
0.4
0.6
0.8
1
d_1/D_j (-)
t/t_{BU} (-)
Exp. Run 1
Exponential fit
(Elasto-capillary model)
d_1/D_j (-)
Exp. Run 1
Exp. Run 2
Exp. Run 3
Exp. Run 4
0.5
t/t_{BU} (-)

Fig. 9

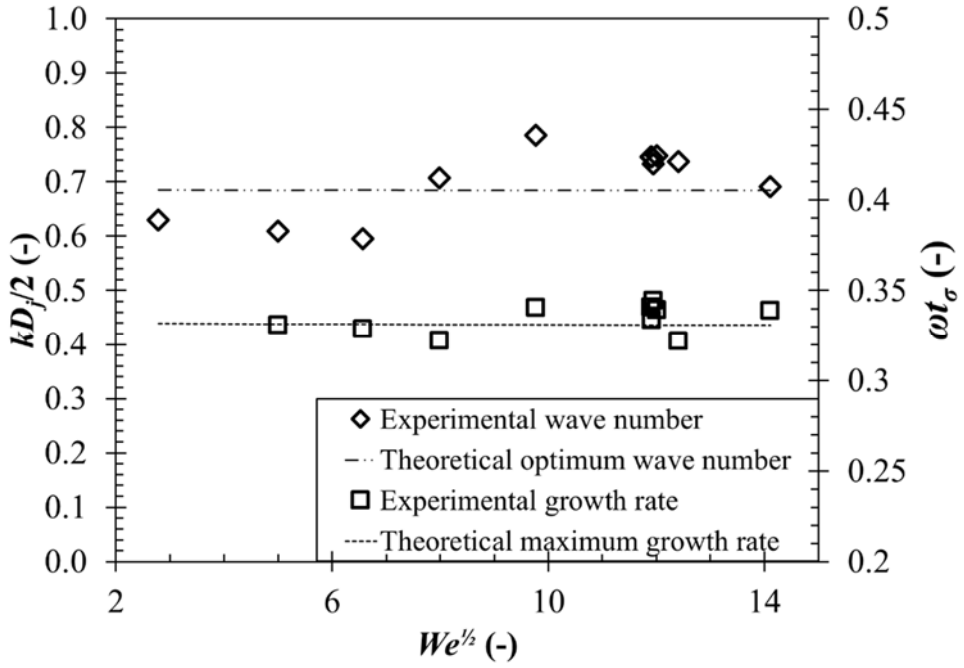
1.0
0.9
0.8
0.7
0.6
0.5
0.4
0.3
0.2
0.1
0.0
0.5
0.45
0.4
0.35
0.3
0.25
0.2
2
6
10
14
$kD_j/2$ (-)
ωt_σ (-)
$We^{1/2}$ (-)
Experimental wave number
Theoretical optimum wave number
Experimental growth rate
Theoretical maximum growth rate

Fig. 10

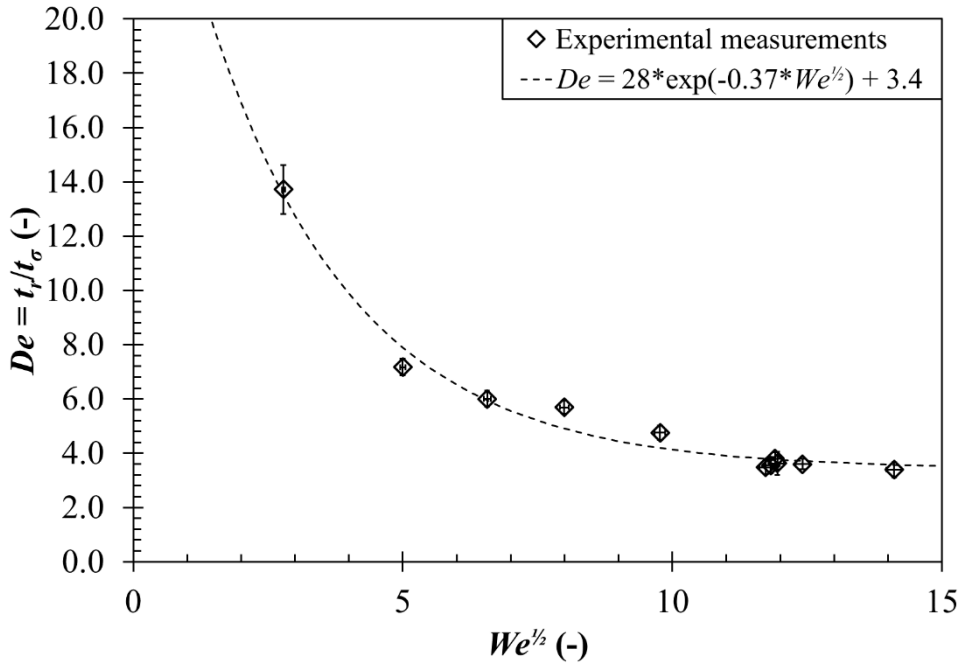
Experimental measurements
De = 28*exp(-0.37*We½) + 3.4
De = tr/tσ (-)
We½ (-)
20.0
18.0
16.0
14.0
12.0
10.0
8.0
6.0
4.0
2.0
0.0
0
5
10
15

Fig. 11

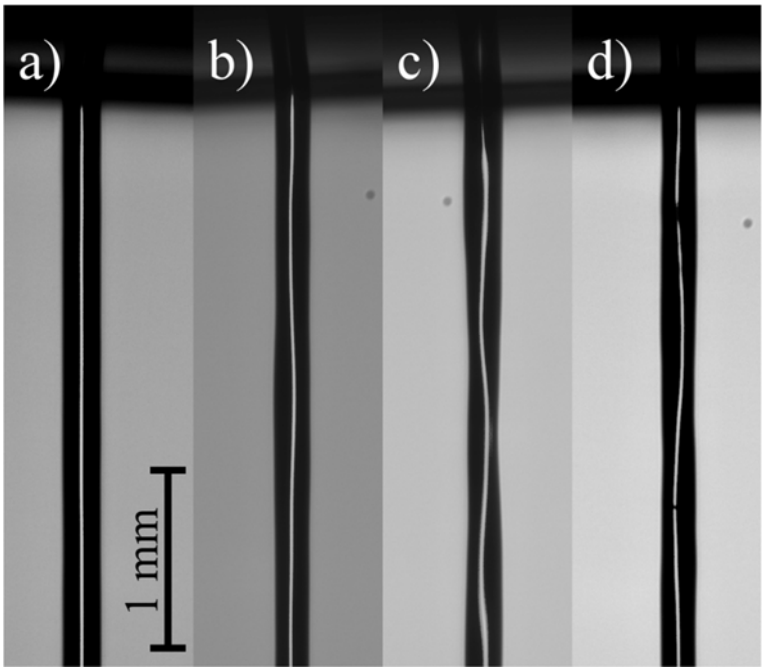

Table 1

Group	Run	D_j (μm)	V_q (m/s)	We ($We^{½}$) (-)
1	1	190	8.58	142 (11.9)
	2	191	8.59	143 (11.9)
	3	192	8.48	140 (11.8)
	4	192	8.42	138 (11.7)
2	5	215	1.89	7.75 (2.78)
	6	206	3.46	25.0 (5.00)
	7	209	4.51	43.1 (6.56)
	8	197	5.66	63.9 (7.99)
	9	193	6.99	95.5 (9.77)
	10	189	8.98	154 (12.4)
	11	184	10.3	199 (14.1)